Drosophila Fog/Cta and T48 pathways have overlapping and distinct contributions to mesoderm invagination

Uzuki Horo[a,†], D. Nathaniel Clarke[a,*], and Adam C. Martin[a,*]
[a]Biology Department, Massachusetts Institute of Technology, 77 Massachusetts Ave, Cambridge, MA 02139

ABSTRACT The regulation of the cytoskeleton by multiple signaling pathways, sometimes in parallel, is a common principle of morphogenesis. A classic example of regulation by parallel pathways is *Drosophila* gastrulation, where the inputs from the Folded gastrulation (Fog)/Concertina (Cta) and the T48 pathways induce apical constriction and mesoderm invagination. Whether there are distinct roles for these separate pathways in regulating the complex spatial and temporal patterns of cytoskeletal activity that accompany early embryo development is still poorly understood. We investigated the roles of the Fog/Cta and T48 pathways and found that, by themselves, the Cta and T48 pathways both promote timely mesoderm invagination and apical myosin II accumulation, with Cta being required for timely cell shape change ahead of mitotic cell division. We also identified distinct functions of T48 and Cta in regulating cellularization and the uniformity of the apical myosin II network, respectively. Our results demonstrate that both redundant and distinct functions for the Fog/Cta and T48 pathways exist.

SIGNIFICANCE STATEMENT

- Morphogenesis involves complex regulation of the cytoskeleton by multiple pathways. Understanding how these pathways contribute to early embryo development remains a challenge.

- Investigating *Drosophila* gastrulation revealed that the Folded gastrulation/Concertina (Fog/Cta) and T48 pathways independently support mesoderm invagination and apical myosin accumulation. Cta is crucial for cell shape changes preceding cell division, with T48 and Cta showing unique roles in cellularization and myosin network organization, respectively.

- This study highlights the redundant and distinct functions of the Fog/Cta and T48 pathways. These findings advance our understanding of morphogenesis regulation and could inform future research into disease mechanisms related to cytoskeletal dysregulation.

INTRODUCTION

During embryonic development, spatially restricted signaling pathways often operate in tandem to elicit cell behaviors (Manning and Rogers, 2014; Burda *et al.*, 2023). Cell shape change, cell motility, and cell division are important cell behaviors that sculpt the embryo (Leptin, 2005; Lecuit *et al.*, 2011; Heisenberg and Bellaïche, 2013). These behaviors are often coordinately regulated by multiple signaling inputs that regulate the cytoskeleton. The actomyosin cytoskeleton, composed of filamentous actin (F-actin) and the nonmuscle myosin-II motor (myosin-II), is a key force generator that drives cell shape change and motility (Vicente-Manzanares *et al.*, 2009). Multiple signaling ligands, receptors, and scaffolds can induce

actomyosin activity, which often interface at a key small GTPase, RhoA (Jaffe and Hall, 2005; Buchsbaum, 2007).

Drosophila gastrulation has been a powerful system to study the impact of cell signaling on RhoA activity (Rho1 in *Drosophila*). During *Drosophila* mesoderm invagination, the spatially restricted expression of *transcript 48* (*t48*) and *folded gastrulation* (*fog*) are required in parallel for mesoderm invagination (Figure 1A; Zusman and Wieschaus, 1985; Costa *et al.*, 1994; Kölsch *et al.*, 2007; Seher *et al.*, 2007). Fog is a GPCR ligand that functions through the G protein-coupled receptors (GPCRs), Mist and Smog, to activate the $G\alpha_{12/13}$ protein Concertina (Cta; Parks and Wieschaus, 1991; Costa *et al.*, 1994; Dawes-Hoang *et al.*, 2005; Manning *et al.*, 2013; Kerridge *et al.*, 2016; Jha *et al.*, 2018). Cta is thought to recruit and/or activate a Rho Guanine nucleotide exchange factor, RhoGEF2, to mediate apical Rho1 activation and cell shape change (Morize *et al.*, 1998; Nikolaidou and Barrett, 2004; Kölsch *et al.*, 2007; Mason *et al.*, 2016). T48 is a transmembrane protein with a PDZ binding motif. T48 is thought to bind RhoGEF2 through RhoGEF2's PDZ domain (Kölsch *et al.*, 2007; Urbansky *et al.*, 2016), although how the function of this interaction cooperates with the Cta-RhoGEF2 interaction is poorly understood. The Fog/Cta pathway is required for coordinated, synchronous apical constriction (Parks and Wieschaus, 1991; Sweeton *et al.*, 1991; Costa *et al.*, 1994; Fox and Peifer, 2007). Furthermore, it is known that Cta is required for timely myosin-II accumulation in cells that initially have a large apical area (Xie *et al.*, 2016). In the *Drosophila* germband, the ectoderm undergoing convergent extension, Cta is required for medioapical myosin-II assembly downstream of RhoGEF2 (Garcia De Las Bayonas *et al.*, 2019). While the Fog/Cta pathway and T48 pathways are known to function in parallel to promote invagination (Kölsch *et al.*, 2007), the individual contributions of each pathway to myosin-II accumulation and function are unclear.

Fog and T48 expression are zygotically controlled by the transcription factor, Twist, which is upstream of the transcription factor Dorsal (Costa *et al.*, 1994; Kölsch *et al.*, 2007). Twist both activates Fog and T48 and delays mesoderm cell division until after invagination via expression of the cell cycle inhibitor, Tribbles (Grosshans and Wieschaus, 2000; Seher and Leptin, 2000). Snail promotes apical myosin II recruitment and cell shape change, in part, by repressing the *Bearded* family of genes (Perez-Mockus *et al.*, 2017). Mist expression is regulated by Snail, and modulated by Twist and Dorsal, while Smog is maternally deposited into the embryo (Manning *et al.*, 2013; Kerridge *et al.*, 2016; Carmon *et al.*, 2021). Interestingly, genes downstream of Dorsal and Twist have a dynamic expression pattern – initiating expression at the ventral midline and starting later at more lateral positions (Lim *et al.*, 2017; Carmon *et al.*, 2021). This ventral-lateral gradient of gene expression is thought to result in a multicellular gradient of T48 protein accumulation, Rho1 activation, and apical myosin II accumulation (Spahn and Reuter, 2013; Heer *et al.*, 2017; Lim *et al.*, 2017; Denk-Lobnig *et al.*, 2021).

Here, we measured the effects of *cta* and *t48* mutants on apical myosin-II dynamics and spatial distribution during mesoderm invagination, in addition to other events in early *Drosophila* embryo development. We found that *cta* and *t48* mutants individually cause a delay in mesoderm invagination relative to midcellularization. For *cta* mutants, this delay reflected slower and more discontinuous accumulation of medioapical myosin-II following the end of cellularization. For *t48* mutants, we found that the delay in apical myosin-II accumulation was due, in part, to a delay in cellularization. In severe cases, the myosin-II delay in *cta* mutants resulted in a conflict between apical constriction and cell division timing, which fully disrupted invagination. Overall, we discovered clear, but separate roles for Cta and T48 branches of the Twist pathway, suggesting distinct mechanisms by which each branch of the pathway regulates myosin-II activity while synergizing to contribute to all downstream effects of Twist expression.

RESULTS

Cta and T48 pathways both promote timely mesoderm invagination

To determine the function of the Fog/Cta and T48 pathways in mesoderm invagination, we examined the dynamics of tissue furrowing in mutants affecting each pathway. For the Fog/Cta pathway, we used *cta* mutants because *cta* is maternal effect and 100% of embryos laid by *cta* mutant mothers are affected regardless of zygotic genotype (Parks and Wieschaus, 1991). For the T48 pathway, we used *t48* mutants, which are homozygous viable (Kölsch *et al.*, 2007), enabling us to collect embryos that are maternal and zygotic *t48* mutant. First, we visualized the timing of invagination relative to cellularization in *t48* and *cta* mutants. We found that both *t48* and *cta* mutants exhibited invagination, but that invagination was delayed (Figure 1B). We quantified this delay by measuring the closure time – the time when the apical surfaces of cells on adjacent sides of the ventral furrow touched – relative to a benchmark time in cellularization (17 μm furrow canal depth, time = 0). This took 21.5 ± 1.14 min in one copy Myo:GFP (sqh::GFP) control embryos, whereas *t48* mutants took 28.4 ± 3.13 min. Two copy Myo:GFP control embryos took 22.26 ± 3.01 min, whereas *cta* mutants took 35.4 ± 7.27 min (Figure 1C). Although both mutants caused delays, *cta* mutants had a greater variability and severity in the invagination phenotype – some embryos completely failed to invaginate and others did so, but often with abnormal morphology and fewer cells internalizing (Figure 1, D and E). In contrast, *t48* mutant embryos consistently invaginated, despite the delay (Figure 1, B, D, and E). Therefore, *cta* and *t48* mutants both delay mesoderm invagination as single mutants, with the delay in *cta* being most severe.

After mesoderm invagination, the internalized cells undergo synchronized mitosis (mitotic domain 10 [MD10] divisions) that occur 28 min after the end of cellularization (Foe, 1989), which corresponds to around 41 min from 17 μm cellularization (Figure 1F). In wild-type, MD10 divisions are not observable at the surface of embryos. In contrast, *cta* mutants that failed to invaginate (i.e., *cta*, severe) most often exhibited MD10 (mesoderm domain) divisions at the embryonic surface, which depleted apical myosin, and reversed apical constriction and tissue furrowing, as observed previously (Figure 1F; Supplemental Videos 1 and 2; Ko *et al.*, 2020). We also observed surface MD10 divisions in *cta* mutants with clear invaginations (i.e., *cta*, mild), because the mesoderm failed to fully internalize (Figure 1F; Supplemental Video 3). The timing of these divisions happened around the time expected for wild-type. We did not assess the timing of domain 10 divisions in W-T and *t48* mutants because our imaging resolution was not sufficient to capture internalized mesoderm tissue, the apical myosin network, and the onset of tissue invagination with sufficient time resolution. Thus, in contrast to *t48* mutants, *cta* mutants sometimes caused a more significant delay that led to a conflict between apical constriction and MD10 cell divisions, which disrupted mesoderm internalization, similar to the effects of premature cell division in a cell cycle regulator mutant (Grosshans and Wieschaus, 2000; Seher and Leptin, 2000).

Cta and T48 pathways are not required for medioapical myosin, but promote timely myosin accumulation

To determine the mechanism that underlies the delay in mesoderm invagination in these mutants, we measured the timing of apical myosin accumulation and its accumulation rate. We used the onset
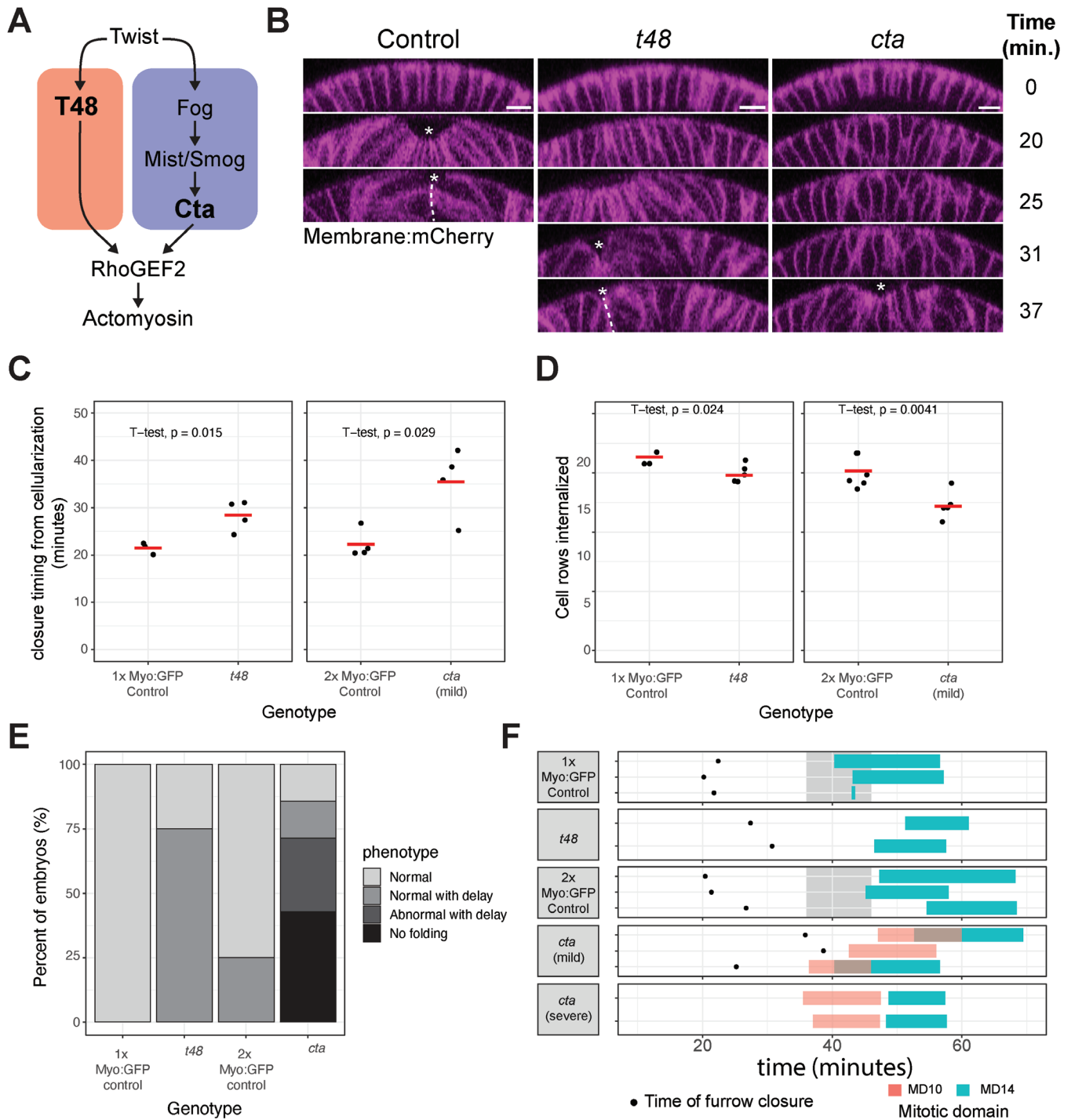
FIGURE 1: Loss of Cta or T48 pathway delays mesoderm invagination respectively. (A) Simplified schematic of the Cta and T48 pathways. (B) Mesoderm invagination of control, *cta, t48* mutant embryos expressing Gap43::mCherry (membrane, magenta). Time = 0 at 17 μm cellularization stage. Scale bar, 10 μm. (C) The completion of mesoderm invagination relative to 17 μm cellularization stage in 1x Myo:GFP (sqh::GFP) control (*n* = 3), *t48* (*n* = 4), 2x Myo:GFP control (*n* = 4), *cta* mild embryos (*n* = 4). (D) Ventral cell rows internalized at the completion of mesoderm invagination in 1x Myo: GFP control (*n* = 3), Myo:GFP; *t48* (*n* = 5), 2x Myo:GFP control (*n* = 6), *cta*; Myo:GFP/Myo:GFP mild embryos (*n* = 6). *cta* mild embryos had partial mesoderm invagination whereas *cta* severe embryos did not fold. (E) Distribution of mesoderm invagination phenotype in terms of morphology and timing in 2x Myo:GFP control (*n* = 4), *cta* (*n* = 7), 1x Myo:GFP control (*n* = 3), *t48* (*n* = 4) embryos. (F) Timing of the completion of mesoderm invagination, mitotic domain 10 (MD10) divisions, and mitotic domain 14 (MD14) divisions. Time = 0 at 17 μm cellularization stage. In 1x Myo:GFP control, *t48*, 2x Myo:GFP control, the timing of MD10 division was estimated based on Foe. 1989 and shown as the grey shading. Statistical comparison in (C and D) were made with Welch's unpaired *t* test.

of apical myosin accumulation as the readout of the start of mesoderm invagination. We found that apical myosin could still accumulate in both *cta* and *t48* mutant embryos (Figure 2A). Consistent with the invagination delay, both *cta* and *t48* mutants resulted in a slower rate of myosin accumulation, leading to lower total levels of myosin in the mesoderm during invagination (Figure 2, A–C). The defect in myosin accumulation was most severe for *cta*, but the delay was also prominent for *t48*, despite the normal appearance of mesoderm invagination in this mutant. Thus, both maternal *cta* and maternal and zygotic *t48* mutants significantly delayed the rate of myosin accumulation.

To determine whether the onset of apical myosin accumulation is also delayed in *cta* and *t48* mutants compared with earlier developmental events, we measured its timing relative to the end of cellularization (i.e., cellularization depth of 30 μm). By tracking the depth of the cellularization front in confocal movies from control and *t48* mutants, we found that the timing of mesoderm invagination was not delayed relative to a cellularization depth of 30 μm (Figure 2D). In contrast, *cta* mutants exhibited a clear delay in apical myosin accumulation relative to the end of cellularization (Figure 2D). These results suggest that the delay in myosin accumulation onset after the end of cellularization can explain the mesoderm invagination delay in *cta* mutants, but not in *t48* mutants. Therefore, we suspected the potential role of T48 in earlier development which might have resulted in the delay in the onset of myosin accumulation in *t48* mutants. Consistent with the earlier role for T48, we found that T48 transcript was ubiquitously present at early stages, as previously described (Urbansky *et al.*, 2016). The presence of ubiquitous, possibly maternal, transcript preceded spatially restricted zygotic gene expression in the center of the Twist expression domain (Figure 2E), implicating the involvement of T48 in developmental events before mesoderm invagination.

Myosin accumulation delay in t48 mutants is, in part, a consequence of a cellularization delay

To determine whether the delay in apical myosin accumulation reflected a cellularization delay in *t48* mutant embryos, we measured the increase in cell height over time in confocal movies. We found a decreased rate of cellularization in *t48* mutants in comparison to controls (Figure 3, A and B). The cellularization rate in *cta* mutants was more variable than that of control or *t48* mutants, however, on average occurred at similar rate as controls (Figure 3B). To understand the relationship between cellularization speed and the onset of myosin accumulation, we measured the correlation between them for *t48* mutants and controls. We found that embryos with lower cellularization speed tended to have greater delay in the onset of myosin accumulation (Figure 3C), suggesting that the mesoderm invagination delay in the *t48* mutant was, at least partly, due to a delay in cellularization.

We verified the cellularization defect in *t48* mutants using stocks that lacked GFP fusion proteins by using brightfield microscopy to visualize furrow canal decent towards the yolk. Cellularization has two phases: an initial slow phase where the furrow descends to ~10 μm depth, and a later fast phase where the furrow canal descends the remaining distance to the yolk (Merrill *et al.*, 1988). Tracking the furrow canal position demonstrated that *t48* mutants undergo the initial slow phase normally but failed to speed up during fast phase for an overall slower cellularization rate (Figure 3, D and E). Notably this defect happened around the entire embryo, consistent with the presence of uniformly distributed *t48* transcripts at this stage (Figure 2E; Urbansky *et al.*, 2016). In addition to the cellularization defect before gastrulation, we found that *t48* mutants

had rounder egg shape (Figure 3F). Taken together, these results showed that the T48 pathway has functions before gastrulation including regulating cellularization and egg shape.

Cta and T48 pathways have distinct effects on the spatial distribution of myosin accumulation across the mesoderm tissue

Given the different effects of *cta* and *t48* mutants during cellularization, we next examined whether there were differences between these mutants in the tissue-wide assembly of the apical myosin network. First, we examined the ventral-to-lateral multicellular gradient of apical myosin. By projecting apical-basal cross section along the anterior-posterior axis, we could measure the ventral-lateral "profile" of the multicellular apical myosin gradient over time (Figure 4, A and B; Supplemental Video 4). Fitting this myosin intensity profile and measuring the half-maximal myosin width demonstrated that disrupting either *cta* or *t48* reduced the multicellular myosin gradient width (Figure 4, C–E). Furthermore, we measured the percent myosin coverage from the ventral midline, and similarly found that the width of the zone covered by myosin was reduced in both *cta* and *t48* mutants (Figure 4, F–I). Taken together, our data demonstrate that both Cta and T48 are individually required to extend the multicellular myosin gradient laterally into the margins of the mesoderm.

While we observed that both *cta* and *t48* affected the width of the myosin gradient, we saw a qualitatively different effect of each pathway on the continuity of the supracellular myosin network (Figure 5, A, B, E, and F). To quantify this observation, we measured the porosity of the myosin signal. Both the mean diameter of pores, and the number of large pores were increased in *cta* mutants relative to the control (Figure 5, C and D). Thus, *cta* reduced myosin accumulation while also resulting in a more discontinuous supracellular myosin network. In contrast, *t48* mutants lowered the amount of myosin accumulation without affecting the visible continuity of the supracellular meshwork (Figure 5, G and H). Taken together, these data showed that while both *cta* and *t48* mutants reduce myosin accumulation rate and the width of the myosin gradient, they affect the organization of the supracellular myosin network differently, likely due to uncoordinated nature of the apical constriction in the *cta* mutant (Sweeton *et al.*, 1991; Xie *et al.*, 2016).

DISCUSSION

The Fog/Cta and T48 pathways function in parallel to promote mesodermal invagination (Kölsch *et al.*, 2007). Despite their redundancy in promoting invagination, we found that each pathway had distinct roles in regulating spatial and temporal apical myosin accumulation and cellularization rate. Disrupting the function of either Cta or T48 delayed myosin accumulation and reduced the width of the multicellular myosin gradient, thus neither pathway is sufficient to reproduce the W-T spatiotemporal profile of apical myosin. While both pathways were required for the normal myosin activation, Cta was uniquely required for uniform myosin activation and coordinated apical constriction across the mesoderm (Parks and Wieschaus, 1991; Sweeton *et al.*, 1991; Xie *et al.*, 2016). Specifically, Cta is required to accumulate apical myosin in cells with larger apical area (Xie *et al.* 2016). In *cta* mutants, although cells with smaller apical area can still accumulate myosin and undergo apical constriction, others with larger apical area cannot, leading to the uncoordinated apical constriction across the mesoderm. The porous myosin networks observed in *cta* mutants likely reflect this uncoordinated apical constriction. Cta was also often required to ensure that cell shape changes and mesoderm invagination preceded mitotic
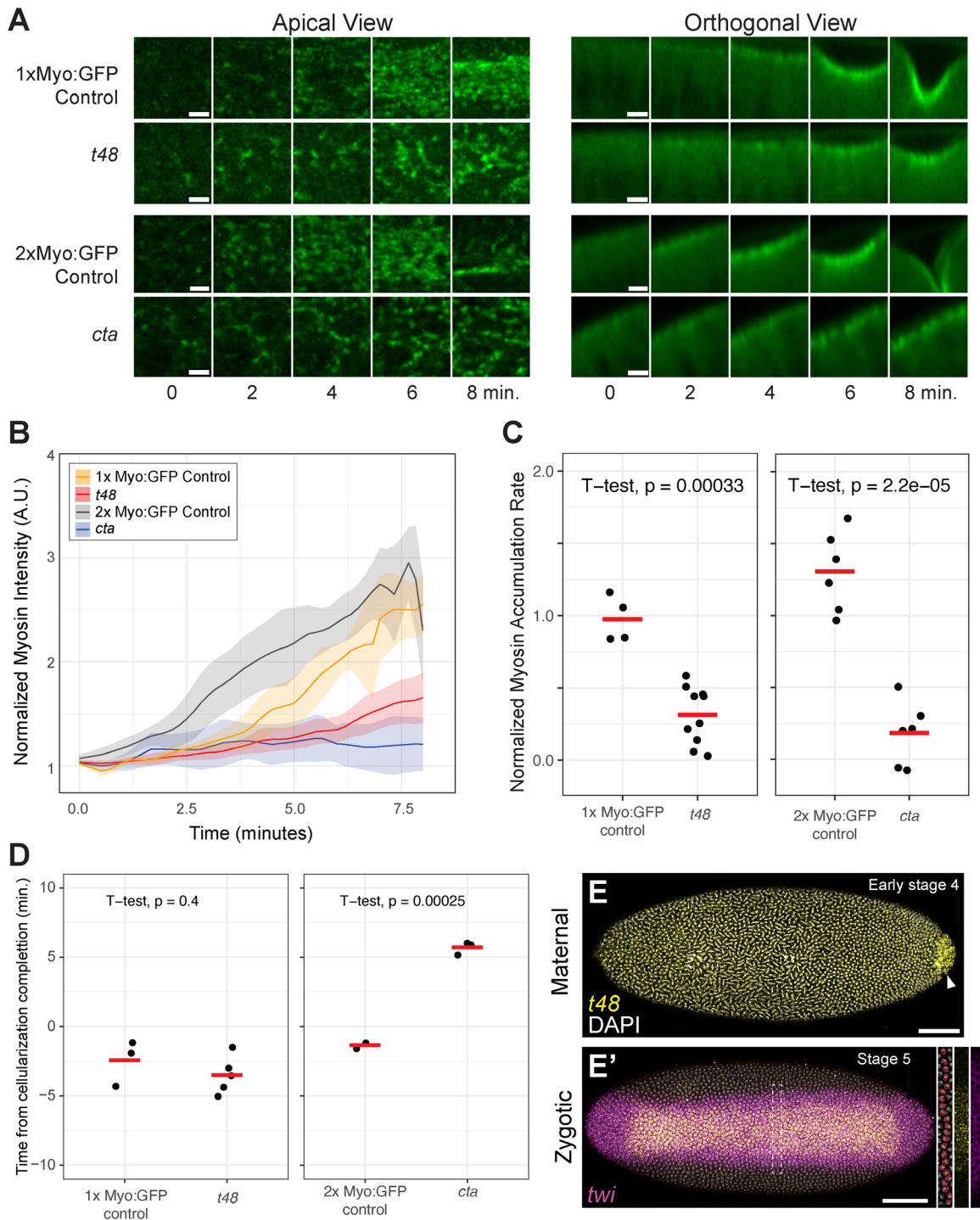
FIGURE 2: Loss of Cta or T48 pathway reduces the myosin accumulation rate during mesoderm invagination.
(A) Time-lapse images of myosin accumulation during mesoderm invagination from both apical and orthogonal view. *cta*
and its control embryos express two copies of Myo:GFP (sqh::GFP, green), whereas *t48* and its control embryos express
one copy of Myo:GFP. Time = 0 at the onset of myosin accumulation. The onset of myosin accumulation was determined
as described in the method section. Scale bars: 5 µm. (B) Quantification of normalized myosin fluorescent intensity at
the ventral midline of two copies Myo:GFP control, *cta* mutant, one copy Myo:GFP control, *t48* mutant embryos. Solid
lines represent mean and shaded area represent plus or minus SD. Time = 0 at the onset of myosin accumulation.
(C) Quantification of normalized myosin accumulation rate during the first 6 min of mesoderm invagination in in
1x Myo:GFP control (*n* = 4) and *t48* (*n* = 10) embryos (left) and 2x Myo:GFP control (*n* = 6) and *cta* (*n* = 6) embryos (right).
(D) Timing of the onset of myosin accumulation from cellularization completion in 1x Myo:GFP control (*n* = 3) and *t48*
(*n* = 5) embryos (left) and 2x Myo:GFP control (*n* = 2) and *cta* (*n* = 3) embryos (right). Statistical comparison in (C and D)
were made with Welch's unpaired *t* test. (E and E′) Fluorescent in situ hybridization for twist and t48 mRNA in early
stage 4 and stage 5 wild-type embryos. Arrowhead points to pole cells. Inset in (E′) shows single-channel images for a
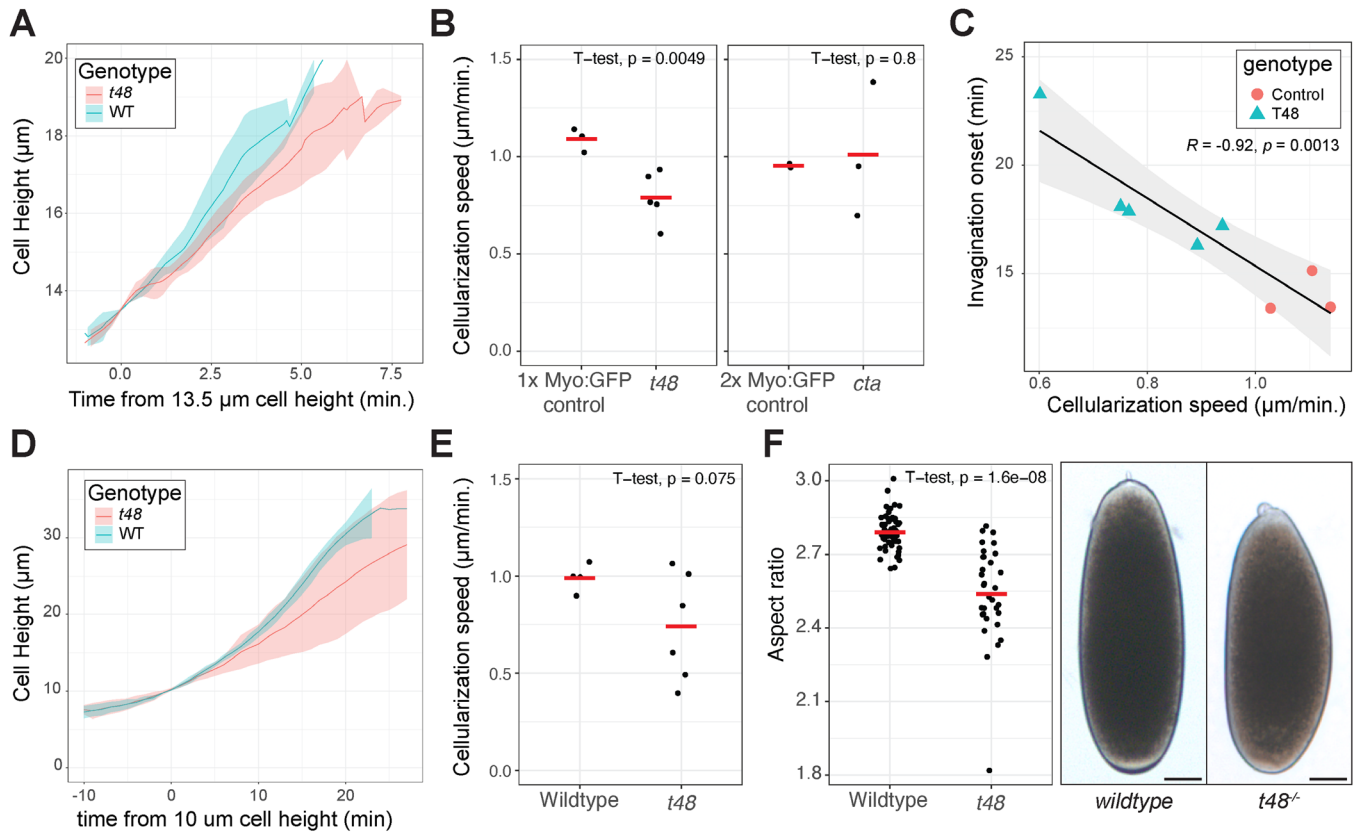single row of cells; nuclei are outlined in red. Scale bar: 50 µm.

FIGURE 3: *t48* mutants exhibit the reduced cellularization speed, which correlates with delayed invagination onset. (A) Cell height dynamics during cellularization based on Myo:GFP localization at the cellularization front. Solid lines represent mean and shaded area represent plus or minus SD. Time = 0 at 13.5 µm cellularization. (B) Quantification of cellularization speed in 1x Myo:GFP control (*n* = 3) and *t48* (*n* = 5) embryos. (C) Correlation between the cellularization speed and the onset of myosin accumulation from 13.5 µm cellularization in 1x Myo:GFP control (*n* = 3) and *t48* (*n* = 5) embryos. *R* and *p* are Pearson correlation coefficient and *p* value. (D) Cell height dynamics during cellularization based on brightfield imaging of cellularization front. Solid lines represent mean and shaded area represent plus or minus SD. Time = 0 at 10 µm cellularization. (E) Quantification of cellularization speed in control (*n* = 4) and *t48* (*n* = 6) embryos without sqh::GFP. (F) Aspect ratio of embryos before or during gastrulation in control (*n* = 54) and *t48* (*n* = 33) without Myo:GFP. Images represent brightfield views of early syncytial embryos laid by indicated genotypes. Scale bar: 50 µm. Statistical comparisons in (B, E, and F) were made with a Welch's unpaired *t* test.

divisions, with *cta* mutants sometimes resulting in a *tribbles*-like reversal of furrowing (Grosshans and Wieschaus, 2000; Seher and Leptin, 2000; Ko *et al.*, 2020). In contrast to *cta*, *t48* mutants exhibited uniform, albeit lower levels of, myosin activation and exhibited a reduced rate of cellularization. Therefore, our study demonstrates that the Fog/Cta and T48 pathways are *partially redundant*, with both overlapping and distinct functions during *Drosophila* early embryo development.

Neither cta, nor t48, mutants resemble twist mutant or fog, t48 double mutant

Twist is required to stabilize apical myosin and maintain constricted cell shape. In the *twist* mutant, cells exhibit apical myosin pulses, but cells fail to transition to a state where myosin accumulates (Xie and Martin, 2015). This failure to stabilize apical myosin is also observed in *fog t48* double knockdown embryos (Martin *et al.*, 2010). While *cta* and *t48* mutants delayed myosin accumulation, apical myosin accumulated and promoted apical constriction to the extent that the mesoderm often invaginated. A consequence of failing to stabilize apical myosin is that *twist* mutants fail to assemble a supracellular apical myosin meshwork that spans the mesoderm (Martin *et al.*, 2010). The anterior-posterior directed tension that is gener-

ated by this meshwork is important for pulling the mesoderm into the embryo (Fierling *et al.*, 2022). The *cta* mutant still forms a supracellular apical myosin network, although it is more porous than the normal embryo, presumably because of the uncoordinated apical construction (Parks and Wieschaus, 1991; Xie *et al.*, 2016; Yevick *et al.*, 2019). The *t48* mutant, despite similarly reducing myosin activation rate, did not result in an uncoordinated apical construction phenotype and assembled a supracellular myosin network. Thus, Fog/Cta and T48 function in parallel to stabilize apical myosin, but have nonredundant functions in promoting timely onset of myosin accumulation. An area of future study will be to understand why the reduced activity through the Twist pathway via Fog/Cta and T48 result in different phenotypes with regards to coordination of apical constriction.

Both *cta* and *t48* mutants reduced the width of the ventral-lateral multicellular myosin gradient, in addition to delaying the onset of accumulation. The timing of *T48* and *mist* transcription onset initiates at nuclei along the ventral midline and progresses laterally (Carmon *et al.*, 2021). Furthermore, there is a gradient in the Pol II recruitment rate for each of these transcription units, which leads to graded activity. We observed T48 expression restricted to the central ~12 cells of the mesoderm domain (Figure 2E', inset). The
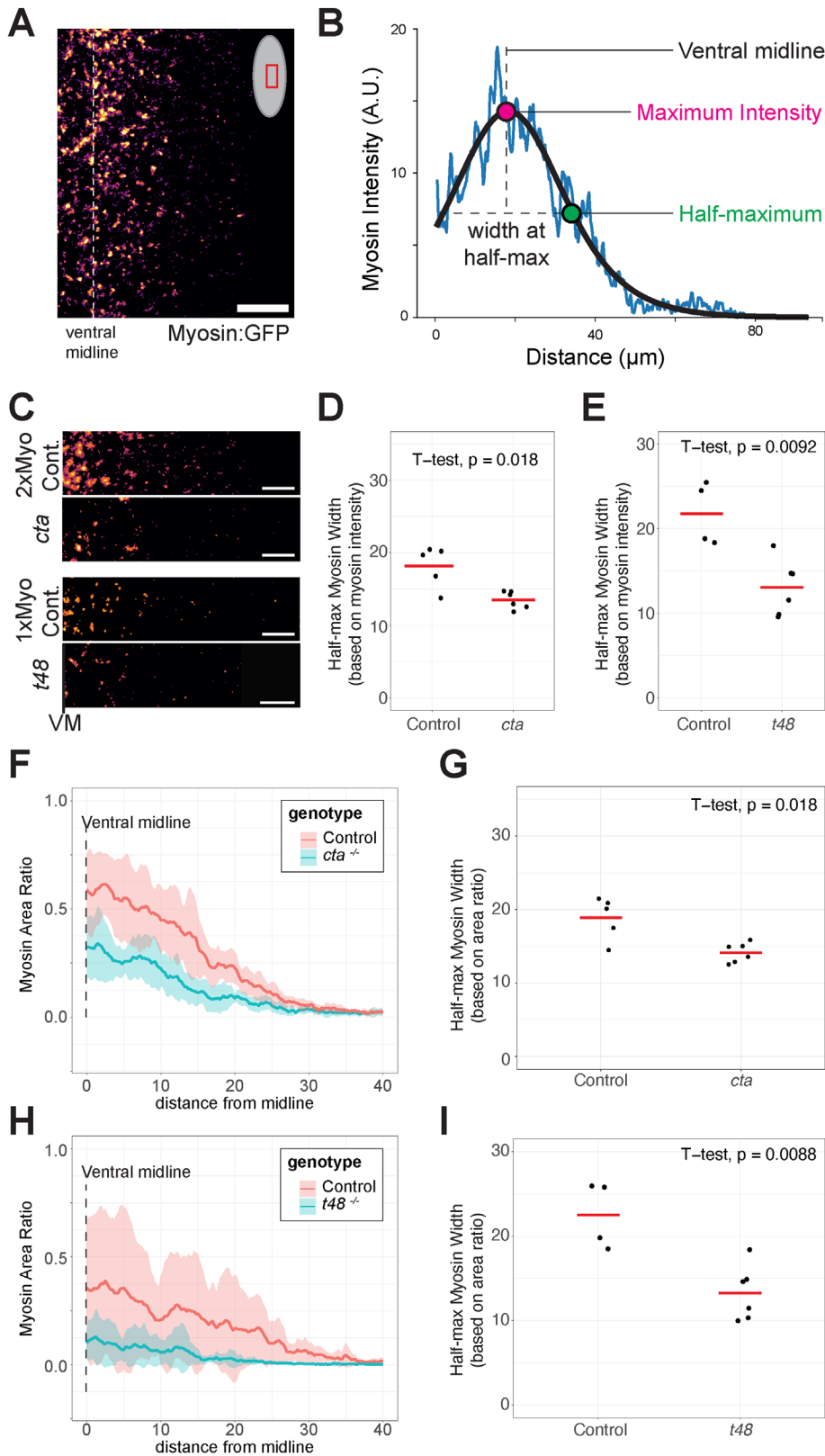
expression of Fog has also been shown to exhibit restricted gene expression to the central ~12 cells of the mesoderm, which corresponds to the zone of greatest apical constriction (Costa et al., 1994). Our results showed that the combined activity of both T48 and the Fog/Mist/Cta pathways are required for the progression of myosin contractility to marginal mesoderm cells. Any one of these pathways is sufficient for the ventral-most cells to apically constrict, however, both pathways are required for the contractile domain to expand to marginal mesoderm cells.

The implications of our study with respect to insect evolution

The loss of Fog/Cta pathway or T48 pathway results in the delay of the completion of mesoderm invagination. Interestingly, there seems to be a correlation between the abundance of mesoderm cells and ventral furrow depth in other insects. In *Tribolium*, mesoderm cell distribution and ventral furrow formation is uneven along the anterior-posterior axis. The anterior region has fewer mesodermal cells and forms a shallower ventral furrow than the posterior (Handel et al., 2005; Benton et al., 2019). In *Chironomus*, *twist*-expressing cells account for around 15% of the embryonic circumference (25% in *Drosophila*) and they form a shallow ventral furrow to internalize mesoderm compared with *Drosophila* (Leptin and Grunewald, 1990; Urbansky et al., 2016). The correlation between the width of mesoderm and the depth of ventral furrow during mesoderm internalization among insects suggests a hypothesis that Fog/Cta pathway and T48 pathway were present in the holometabolous insect ancestor, and their activated regions evolved in different insect lineages with different mesoderm distribution before gastrulation. Indeed, *fog* knockdown in *Tribolium* resulted in slower mesoderm

embryos averaged over 2 min preceding apical flattening. (E) Same quantification as (D) in 1x Myo:GFP control (n = 4) and *t48* (n = 6) embryos. (F and H) The ratio of area with myosin accumulation is calculated for the ventral-lateral axis. Solid lines represent mean and shaded area represent plus or minus SD. (G) Quantification of the average half-max myosin width based on myosin area ratio in (F). 2x Myo:GFP control (n = 5) and *cta* (n = 6) embryos averaged over 2 min preceding apical flattening. (I) Same quantification as (G) in 1x Myo:GFP control (n = 4) and *t48* (n = 6) embryos. Statistical comparisons in (D, E, G, and I) were made with a Welch's unpaired *t* test.

FIGURE 4: Loss of cta or t48 pathway narrows multicellular mesoderm myosin gradient. (A) Representative apical image of myosin accumulation in a 2x Myo:GFP control embryo at the apical flattening stage. Scale bar: 20 μm. (B) Myosin intensity profile from the ventral-lateral axis and a fitted curve of (A). Half-max myosin width is the distance between maximum myosin intensity position and half maximum myosin intensity position of the fitted curve. (C) Representative images of apical myosin gradients in *cta* and *t48* mutants relative to control. (D) Quantification of the half-max myosin width of 2x Myo:GFP control (n = 5) and *cta* (n = 6)
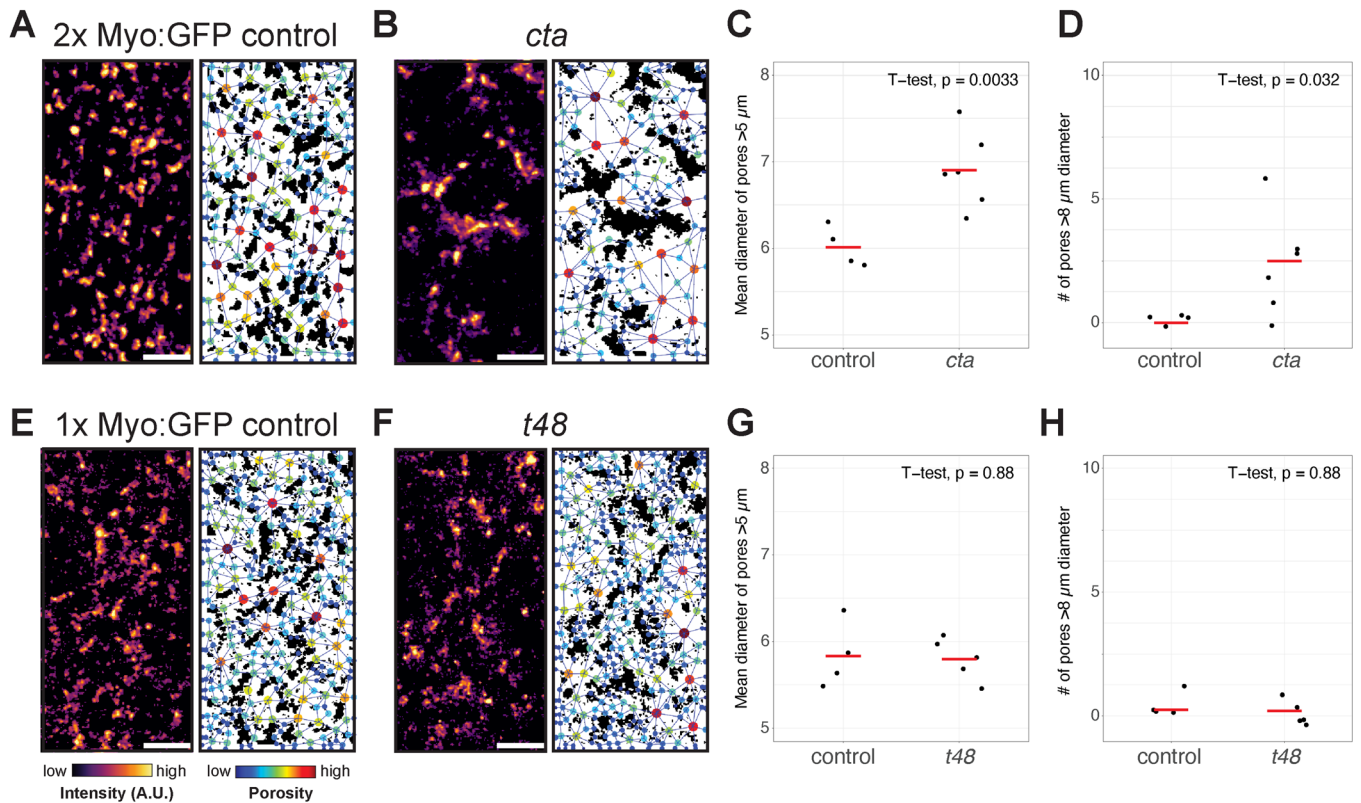
FIGURE 5: Loss of cta pathway, but not t48 pathway, results in porous supracellular myosin network. (A, B, E, and F) Representative apical images of supracellular myosin network and pore distribution in 2x Myo:GFP control (A), *cta* (B), 1x Myo:GFP control (E), *t48* embryo (F). Left: myosin distribution at the center of mesoderm (60 um in anterior-posterior axis, 30 μm in dorsal-ventral axis). Right: significant myosin accumulation is present in black regions. Pore networks inferred from white regions are overlayed. The colors of nodes in pore network represent the diameter of each inferred pore. Scale bars: 10 μm. (C) The mean diameter of pores greater than 5 μm for each embryo of 2x Myo:GFP control ($n = 4$) and *cta* ($n = 6$) at the apical flattening stage. (D) Number of pores with greater than 8-μm diameter in each embryo of 2x Myo:GFP control ($n = 4$) and *cta* ($n = 6$) embryos at the apical flattening stage. (G) Same quantification as (C) for 1x Myo:GFP control ($n = 4$) and *t48* ($n = 5$) embryos. (H) Same quantification as (D) for 1x Myo:GFP control ($n = 4$) and *t48* ($n = 5$) embryos. Statistical comparison in (C, D, G, and H) were made with Welch's unpaired t test.

internalization and a shallower ventral furrow in the posterior mesoderm (Benton *et al.*, 2019). Furthermore, the overexpression of *fog* and *t48* in *Chironomus* increased the number of internalized mesoderm cells (Urbansky *et al.*, 2016). Collectively, these studies and our own suggest a conserved function of Fog/Cta and T48 pathways in modulating mesoderm internalization among insects.

In *Drosophila*, the gradients of Fog/Cta and T48 pathway activities from the ventral midline are regulated by the gradient of nuclear Dorsal that contrasts with the uniform expression of *twist* at stages immediately preceding gastrulation (Carmon *et al.*, 2021). In *Tribolium*, *fog* expression does not form a gradient from the ventral midline; rather it appears to peak at the periphery of mesoderm (Benton *et al.*, 2019). A similar expression pattern is observed in *Chironomus fog2* (Urbansky *et al.*, 2016). The peripheral expression pattern of *fog* is counterintuitive because the ventral furrow forms along the ventral midline in both insects. In *Chironomus*, but not *Tribolium*, *mist* is expressed along the ventral midline which may partly explain how Fog/Mist/Cta pathway activation is restricted to the ventral midline. How *fog* expression is regulated across mesoderm in other insects remain unclear. Although *Toll* knockdown in *Tribolium* results in the loss of *fog* expression in the mesoderm, *twist* knockdown does not change *fog* expression, suggesting a different *fog* expression regulation mechanism from *Drosophila*. Interestingly, the persistence of the Dorsal nuclear gradient during cellularization and early

gastrulation is not conserved in *Tribolium* (Chen *et al.*, 2000). Dorsal accumulates uniformly across the mesoderm along with weak *twist* expression in the beginning. Then, the Dorsal nuclear gradient gets narrower and ultimately disappears. During ventral furrow formation, only weak cytoplasmic signal is detected in the mesoderm except for the primitive pit. Despite the narrowing of Dorsal nuclear gradient, Twist continues to be expressed across mesoderm during ventral furrow formation (Handel *et al.*, 2005). The peripheral expression of *fog* in the mesoderm of basal insects and its relation to the mechanisms mesoderm internalization is an area of future interest.

There are multiple hypotheses on the ancestral function of Fog/Cta pathway and/or T48 pathway. One hypothesis proposes that *fog* and *t48* had ancestral roles in the later epithelial morphogenesis which was then coopted in early development (Urbansky *et al.*, 2016). In addition to early development, the Fog/Cta pathway is involved in epithelial morphogenesis in later developmental events such as wing, leg, and salivary gland formation (Nikolaidou and Barrett, 2004; Ratnaparkhi and Zinn, 2007; Manning *et al.*, 2013). Furthermore, *fog* and *t48* are present among winged insects whereas their homologues have not been found in nonwinged insects to date, implying their ancestral function in later development including wing morphogenesis (Urbansky *et al.*, 2016).

Another hypothesis argues that the ancestral function of Fog/Cta pathway is in blastoderm formation (Benton *et al.*, 2019). In

addition to the abnormal myosin dynamics during mesoderm invagination, we showed that *t48* mutants exhibited slower cellularization speed and rounder egg morphology. Publicly available single-cell transcriptome data shows the expression of *t48* in the somatic cells of the ovariole, suggesting a potential role of T48 in both early embryogenesis and oogenesis (Li *et al.*, 2022). Although the involvement of T48 pathway before mesoderm invagination is not known in other insects, Fog/Cta pathway is required for the blastoderm formation in multiple insect species including *Tribolium* (Benton *et al.*, 2019). Publicly available *Tribolium* transcriptome data shows the enrichment of *t48* in female gonad albeit in less degree compared with *fog* (Naseem *et al.*, 2023). Given that T48 facilitates Fog/Cta pathway during mesoderm invagination in *Tribolium* (Benton *et al.*, 2019), it is conceivable that T48 pathway also plays a role in blastoderm formation and/or oogenesis. We showed that in *cta* mutants of *Drosophila*, although the average cellularization speed was not different from control, there is a greater variability. Further study is needed to reveal the role of Cta in cellularization of the *Drosophila* embryo. Moreover, previous work showed that *cta* mutants of *Drosophila* show abnormal nuclear position and greater variability in apical cell area before apical constriction (Xie *et al.*, 2016). Therefore, we are more inclined toward the hypothesis that the involvement of Fog/Cta and T48 pathways in blastoderm formation is ancestral and conserved among insect species. However, *Tribolium*, *Chironomus*, and *Drosophila* are the only species studied with functional analysis of both Fog/Cta and T48 pathways to date. Future studies in broader insect species are necessary to reveal the evolution of Fog/Cta and T48 pathway in the early embryogenesis.

MATERIALS AND METHODS

Fly stocks and crosses

For *t48* mutants, *t48* was maintained as homozygous stocks with myosin (Sqh::GFP) and membrane (Gap43::mCherry) markers present on the second chromosome. The Sqh::GFP; *t48* flies failed to lay viable embryos. Therefore, embryos from Sqh::GFP/Cyo; *t48* and Gap43::mCherry/Cyo; *t48* flies were used to image myosin and membrane, respectively. Single copy myosin controls were embryos from SqhGFP, Gap43::mCherry/Cyo flies.

For *cta* mutants, *cta* was placed over a deficiency (pr31) to examine the maternal effect phenotype of resulting embryos from homozygous *cta* mutant mothers. Briefly *cta*/CyO flies were crossed to pr31/CyO; Sqh::GFP, Gap43::mCherry/TM3 or pr31/CyO; Sqh::GFP. The *cta*/pr31; Sqh::GFP, Gap43::mCherry/Sqh::GFP females or *cta*/pr31; Sqh::GFP/Sqh::GFP flies were collected and crossed to sibling males. Resulting embryos were imaged. For controls with the same copy number of Sqh::GFP, SqhGFP flies were crossed to SqhGFP, Gap43::mCherry/Cyo. SqhGFP/SqhGFP, Gap43::mCherry files were collected and crossed to sibling males. Resulting embryos were imaged.

Embryonic lethality analysis

Adult flies were allowed to lay eggs for 3–6 h on apple juice-containing agar plate and the number of eggs were counted. After more than 24 h, the number of eggs that did not hatch were counted as embryonic lethal. The survival rate of embryo was calculated as 1 – (# of eggs did not hatch/# of total eggs).

Live imaging (confocal, brightfield)

We collected embryos on apple juice plates and immersed them in Halocarbon 27 oil (Sigma) for staging. We collected blastoderm stage embryos and prepared them for imaging.

For confocal imaging, we dechorionated embryos with 50% bleach, rinsed them with water, and mounted them ventral side up on a slide coated with embryo glue (Scotch tape glue resuspended in heptane, coated onto slide, and allowed to dry). We made a chamber for the glued embryos with No. 1.5 coverslip spacers and a No. 1.0 top coverslip and filled the chamber with Halocarbon 27 oil. We acquired images on a Zeiss LSM710 microscope with an Apochromat 40x/1.2 numerical aperture W Korr M27 objective at room temperature.

For brightfield imaging, we placed embryos with chorion onto a slide with Halocarbon 27 oil and imaged them with brightfield optics using a Nikon 10x/0.25 numerical aperture objective or a Nikon LWD 20x/0.40 numerical aperture objective.

Image processing and analysis

Images in Figures 1 and 2 were processed using Fiji and those in Figures 4 and 5 were processed using Python 3.9.18. Specific adjustments are described for specific analyses and figure panels below.

Morphological analysis of mesoderm invagination

In Figure 1B, membrane channel was processed with a gaussian blur with a radius of 1 pixel and resliced to generate orthogonal views. The timing of 17-µm cellularization, the closure of the furrow and the number of cell rows internalized were manually determined by examining both apical view and orthogonal view images. The morphological phenotype of invagination was manually determined. Embryos which did the closure of the furrow more than 26 min later than 17 µm cell height were categorized as delayed (Figure 1E). Timing of mitotic domain 10 (MD10) and 14 (MD14) divisions were manually determined by examining both apical view and orthogonal view images. Because MD 10 divisions occur in internalized mesoderm in control and *t48* mutant embryos they were not measured and the estimated timing from the literature was used instead. In *cta* mutant embryos, MD14 divisions were distinguished from MD10 divisions based on their relative location in embryo and the division angle. Most MD14 divides in anterior-posterior axis and forms a row of cells, whereas most MD10 divides in apical-basal axis. (Figure 1F)

Myosin accumulation during mesoderm invagination

In Figure 2A, the myosin channel was processed with a Gaussian blur with a radius of 1 pixel. Apical views were obtained by maximum z projection over full stack. To obtain orthogonal views, images were resliced and underwent average Z-projection over 20 µm along anterior-posterior axis. To display myosin intensity differences, contrasts were adjusted by setting the minimum and maximum values. The same adjustments were made for images that were compared.

Quantification of myosin accumulation at the ventral midline

For analyzing myosin intensity at ventral midline, myosin channel was processed with a gaussian blur with a radius of 1 pixel. Next, images were resliced and underwent average Z-projection over 20-µm along anterior-posterior axis. Then, linear ROIs were drawn to measure myosin intensity profile along apical-basal axis of cells at the ventral midline. The maximum intensity and its position of each myosin profile was obtained. The position was obtained by calculating the position of maximum myosin from that of vitelline membrane. The autofluorescent vitelline membrane position was obtained by finding the first position at which GFP channel intensity is greater than background signal (2.5 was used as a threshold for all embryos).

During mesoderm invagination, myosin intensity is maximum at the apical surface. Therefore, apical myosin intensity was obtained from the maximum myosin intensity. For each embryo, three apical myosin intensity were obtained from different ROIs and averaged to obtain final apical myosin intensity.

In Figure 2, images were aligned at the onset of apical myosin accumulation during mesoderm invagination. The onset of myosin accumulation was defined as the timing when myosin intensity at the apical surface became greater than mean cytoplasmic myosin intensity plus two SD. Mean cytoplasmic myosin intensity and SD was obtained from a rectangle ROI selecting cytoplasm for each embryo. The apical myosin intensity was then normalized to the threshold for quantification (Figure 2, B–D).

Cell height measurements during cellularization

For cellularization analysis using confocal microscopy, embryos with less than 14-μm cell height at the start of image acquisition and exhibited at least 5 μm increase in cell height were used to capture enough cellularization dynamics. The position of maximum myosin intensity during cellularization was used as the cell height of embryos. This is because during cellularization, myosin intensity is maximum at the cellularization front. (Figure 3, A and B)

For cellularization analysis using brightfield microscopy, embryos with less than 10-μm cell height at the start of image acquisition were used to capture cellularization dynamics. The cell height of the initial frame was manually measured and the movement of cellularization front was tracked by Manual Tracking plugin in Fiji. Measurement and tracking were done three times per embryo and the average cell height at each frame was calculated using R script (Figure 3D).

Aspect ratio of embryos

To measure aspect ratio of embryos, brightfield images were converted to eight-bit. To segment embryos, 0 to 200-pixel value was used as threshold. Aspect ratio of segmented embryos was measured using "Analyze Particles" in Fiji with the option "size = 100-Infinity" to exclude debris (Figure 3F).

Myosin network extraction

Custom Python and R scripts were used to analyze myosin gradient width and pore characteristics of myosin network (Figure 4). Images were first rotated to have ventral side en face and processed with a Gaussian filter with 1 pixel size. To extract myosin network, cytoplasmic background signal was subtracted by setting pixel values with smaller than mean plus two SD cytoplasmic myosin intensity to zero. To obtain cytoplasmic myosin intensity, image frame with no myosin accumulation was manually selected, processed with a gaussian filter with 3 pixel size and background signal (smaller than 2.5 pixels) was subtracted. Two-dimensional myosin network was obtained by conducting maximum intensity Z-projection of the extracted myosin network (Figure 4A). The myosin networks at the apical flattening stage were used in Figures 4 and 5.

Myosin intensity profile

Myosin intensity profiles along the ventral-lateral axis were generated by averaging myosin intensity of two-dimensional myosin network over anterior-posterior axis (Figure 4B). To quantitatively compare the gradient of myosin profile, the myosin profiles were fit to a function as in (Denk-Lobnig et al., 2021):

$$y = a \times 0.5 \times \left(1 + \tanh\left(s\left(x - \left(x_0 - 0.5 \times w\right)\right)\right)\right) \times 0.5$$
$$\times \left(1 + \tanh\left(-s\left(x - \left(x_0 + 0.5 \times w\right)\right)\right)\right)$$

where y corresponds to myosin profile and x corresponds to the position in ventral-lateral axis. Optimal variables were found using curve fit function of scipy.optimize in scipy.1.11.2. Upper and lower limits and initial guesses for each variable were as follows: a: 0, 255, 10; s: 0, 30, 3; w: 0, infinity, 20; x0: -infinity, infinity, manually specified value compatible with the position of ventral midline of each embryo. The distance between maximal myosin intensity and half-maximal myosin intensity of the fitted function was used as the width of myosin gradient. To smooth the fluctuations in myosin gradient width over the time course, the half-maximal myosin width at a given time was averaged with the time steps before and after.

Myosin area ratio profile

Myosin area ratio profile from ventral midline to the lateral was obtained by calculating the ratio of pixels with myosin accumulation over anterior-posterior axis (Figure 4, E and G). Myosin gradient widths were found by fitting the same function as used for myosin intensity profile with the following initial guesses for each variable: a: 1, s: 3, w: 20, x0: the same manually specified value as in myosin intensity profile. To smooth the fluctuations in the myosin gradient over the time course, the half-maximal myosin width of at a given time was averaged with the time steps before and after.

Myosin network pore size and distribution

To measure size and distribution of pores in myosin network, we used PoreSpy 2.3.0 package (Gostick et al., 2019) in Python 3.9.18. Myosin network images that cover at least 15 μm from ventral midline to both left and right sides were selected. To remove the effect of myosin covered area ratio on pore size, myosin network images were binarized with a new threshold such that myosin covered area ratio equaled to 0.25 at the apical flattening stage of each embryo. To detect pores in binarized myosin network images, the SNOW algorithm implemented in PoreSpy was applied with voxel size = 1. (https://porespy.org/examples/networks/tutorials/snow_basic.html). The identified pore network was overlayed on the myosin network images using visualization functions of PoreSpy.

Statistics

To statistically compare means of two independent groups whose variance were not assumed to be equal, Welch two sample t test were performed using ggplot2-3.4.4. Normality of sample distribution was tested using Shapiro-test in R.

Fluorescent in situ hybridization

To detect twist and t48 RNA transcripts, we used the hybridization chain reaction (HCR) method, version 3.0 (Choi et al., 2018). We designed ~30 probe pairs for each gene targeting the coding sequence and portions of the UTRs, depending on gene length. Probes were ordered as pooled libraries (OligoPools, Integrated DNA Technologies) and resuspended in nuclease-free water at a concentration of 0.5 μM. Alexa-Fluor-conjugated detection hairpins were acquired from Molecular Instruments. HCR in situ hybridization was performed according to the manufacturer's protocol using standard formaldehyde-methanol fixed embryos. Following staining, embryos were postfixed for 15 min in 4% paraformaldehyde, and mounted in AquaPolymount. Expression patterns were validated against previously published patterns for both genes.

REFERENCES

Benton MA, Frey N, Nunes da Fonseca R, von Levetzow C, Stappert D, Hakeemi MS, Conrads KH, Pechmann M, Panfilio KA, Lynch JA, *et al.* (2019). Fog signaling has diverse roles in epithelial morphogenesis in insects. eLife 8, e47346.

Buchsbaum RJ (2007). Rho activation at a glance. Journal of Cell Science 120, 1149–1152.

Burda I, Martin AC, Roeder AHK, Collins MA (2023). The dynamics and biophysics of shape formation: Common themes in plant and animal morphogenesis. Dev Cell 58, 2850–2866.

Carmon S, Jonas F, Barkai N, Schejter ED, Shilo B-Z (2021). Generation and timing of graded responses to morphogen gradients. Development 148, dev199991.

Chen G, Handel K, Roth S (2000). The maternal NF-kappaB/dorsal gradient of Tribolium castaneum: dynamics of early dorsoventral patterning in a short-germ beetle. Development 127, 5145–5156.

Choi HMT, Schwarzkopf M, Fornace ME, Acharya A, Artavanis G, Stegmaier J, Cunha A, Pierce NA (2018). Third-generation in situ hybridization chain reaction: Multiplexed, quantitative, sensitive, versatile, robust. Development 145, dev165753.

Costa M, Wilson ET, Wieschaus E (1994). A putative cell signal encoded by the folded gastrulation gene coordinates cell shape changes during *Drosophila* gastrulation. Cell 76, 1075–1089.

Dawes-Hoang RE, Parmar KM, Christiansen AE, Phelps CB, Brand AH, Wieschaus EF (2005). Folded gastrulation, cell shape change, and the control of myosin localization. Development 132, 4165–4178.

Denk-Lobnig M, Totz JF, Heer NC, Dunkel J, Martin AC (2021). Combinatorial patterns of graded RhoA activation and uniform F-actin depletion promote tissue curvature. Development 148, dev199232.

Fierling J, John A, Delorme B, Torzynski A, Blanchard GB, Lye CM, Popkova A, Malandain G, Sanson B, Étienne J, *et al.* (2022). Embryo-scale epithelial buckling forms a propagating furrow that initiates gastrulation. Nat Commun 13, 3348.

Foe VE (1989). Mitotic domains reveal early commitment of cells in *Drosophila* embryos. Development 107, 1–22.

Fox DT, Peifer M (2007). Abelson kinase (Abl) and RhoGEF2 regulate actin organization during cell constriction in *Drosophila*. Development 134, 567–578.

Garcia De Las Bayonas A, Philippe J-M, Lellouch AC, Lecuit T (2019). Distinct RhoGEFs activate apical and junctional contractility under control of G proteins during epithelial morphogenesis. Curr Biol 29, 3370–3385.e7.

Gostick JT, Khan ZA, Tranter TG, Kok MDR, Agnaou M, Sadeghi M, Jervis R (2019). PoreSpy: A Python toolkit for quantitative analysis of porous media images. J Open Source Softw 7, 1296.

Grosshans J, Wieschaus E (2000). A genetic link between morphogenesis and cell division during formation of the ventral furrow in *Drosophila*. Cell 101, 523–531.

Handel K, Basal A, Fan X, Roth S (2005). Tribolium castaneum twist: Gastrulation and mesoderm formation in a short-germ beetle. Dev Genes Evol 215, 13–31.

Heer NC, Miller PW, Chanet S, Stoop N, Dunkel J, Martin AC (2017). Actomyosin-based tissue folding requires a multicellular myosin gradient. Development 144, 1876–1886.

Heisenberg C-P, Bellaïche Y (2013). Forces in tissue morphogenesis and patterning. Cell 153, 948–962.

Jaffe AB, Hall A (2005). Rho GTPases: biochemistry and biology. Annu Rev Cell Dev Biol 21, 247–269.

Jha A, van Zanten TS, Philippe J-M, Mayor S, Lecuit T (2018). Quantitative control of GPCR organization and signaling by endocytosis in epithelial morphogenesis. Curr Biol 28, 1570–1584.e6.

Kerridge S, Munjal A, Philippe J-M, Jha A, de las Bayonas AG, Saurin AJ, Lecuit T (2016). Modular activation of Rho1 by GPCR signalling imparts polarized myosin II activation during morphogenesis. Nat Cell Biol 18, 261–270.

Ko CS, Kalakuntla P, Martin AC (2020). Apical constriction reversal upon mitotic entry underlies different morphogenetic outcomes of cell division. Mol Biol Cell 31, 1663–1674.

Kölsch V, Seher T, Fernandez-Ballester GJ, Serrano L, Leptin M (2007). Control of *Drosophila* gastrulation by apical localization of adherens junctions and RhoGEF2. Science 315, 384–386.

Lecuit T, Lenne P-F, Munro E (2011). Force generation, transmission, and integration during cell and tissue morphogenesis. Annu Rev Cell Dev Biol 27, 157–184.

Leptin M (2005). Gastrulation movements: The logic and the nuts and bolts. Dev Cell 8, 305–320.

Leptin M, Grunewald B (1990). Cell shape changes during gastrulation in *Drosophila*. Development 110, 73–84.

Li H, Janssens J, De Waegeneer M, Kolluru SS, Davie K, Gardeux V, Saelens W, David FPA, Brbić M, Spanier K, *et al.* (2022). Fly Cell Atlas: A single-nucleus transcriptomic atlas of the adult fruit fly. Science 375, eabk2432.

Lim B, Levine M, Yamazaki Y (2017). Transcriptional prepatterning of *Drosophila* gastrulation. Curr Biol 27, 286–290.

Manning AJ, Peters KA, Peifer M, Rogers SL (2013). Regulation of epithelial morphogenesis by the G protein-coupled receptor mist and its ligand fog. Sci Signal 6, ra98.

Manning AJ, Rogers SL (2014). The Fog signaling pathway: Insights into signaling in morphogenesis. Dev Biol 394, 6–14.

Martin AC, Gelbart M, Fernandez-Gonzalez R, Kaschube M, Wieschaus EF (2010). Integration of contractile forces during tissue invagination. J Cell Biol 188, 735–749.

Mason FM, Xie S, Vasquez CG, Tworoger M, Martin AC (2016). RhoA GTPase inhibition organizes contraction during epithelial morphogenesis. J Cell Biol 214, 603–617.

Merrill PT, Sweeton D, Wieschaus E (1988). Requirements for autosomal gene activity during precellular stages of *Drosophila melanogaster*. Development 104, 495–509.

Morize P, Christiansen AE, Costa M, Parks S, Wieschaus E (1998). Hyperactivation of the folded gastrulation pathway induces specific cell shape changes. Development 125, 589–597.

Naseem MT, Beaven R, Koyama T, Naz S, Su S-Y, Leader DP, Klaerke DA, Calloe K, Denholm B, Halberg KV (2023). NHA1 is a cation/proton antiporter essential for the water-conserving functions of the rectal complex in Tribolium castaneum. Proc Natl Acad Sci USA 120, e2217084120.

Nikolaidou KK, Barrett K (2004). A Rho GTPase signaling pathway is used reiteratively in epithelial folding and potentially selects the outcome of Rho activation. Curr Biol 14, 1822–1826.

Parks S, Wieschaus E (1991). The *Drosophila* gastrulation gene concertina encodes a G alpha-like protein. Cell 64, 447–458.

Perez-Mockus G, Mazouni K, Roca V, Corradi G, Conte V, Schweisguth F (2017). Spatial regulation of contractility by Neuralized and Bearded during furrow invagination in *Drosophila*. Nat Commun 8, 1594.

Ratnaparkhi A, Zinn K (2007). The secreted cell signal Folded Gastrulation regulates glial morphogenesis and axon guidance in *Drosophila*. Dev Biol 308, 158–168.

Seher TC, Leptin M (2000). Tribbles, a cell-cycle brake that coordinates proliferation and morphogenesis during *Drosophila* gastrulation. Curr Biol 10, 623–629.

Seher TC, Narasimha M, Vogelsang E, Leptin M (2007). Analysis and reconstitution of the genetic cascade controlling early mesoderm morphogenesis in the *Drosophila* embryo. Mech Dev 124, 167–179.

Spahn P, Reuter R (2013). A vertex model of *Drosophila* ventral furrow formation. PLoS One 8, e75051.

Sweeton D, Parks S, Costa M, Wieschaus E (1991). Gastrulation in *Drosophila*: The formation of the ventral furrow and posterior midgut invaginations. Development 112, 775–789.

Urbansky S, González Avalos P, Wosch M, Lemke S (2016). Folded gastrulation and T48 drive the evolution of coordinated mesoderm internalization in flies. eLife 5, e18318.

Vicente-Manzanares M, Ma X, Adelstein RS, Horwitz AR (2009). Nonmuscle myosin II takes centre stage in cell adhesion and migration. Nat Rev Mol Cell Biol 10, 778–790.

Xie S, Martin AC (2015). Intracellular signalling and intercellular coupling coordinate heterogeneous contractile events to facilitate tissue folding. Nat Commun 6, 7161.

Xie S, Mason FM, Martin AC (2016). Loss of Gα12/13 exacerbates apical area dependence of actomyosin contractility. Mol Biol Cell 27, 3526–3536.

Yevick HG, Miller PW, Dunkel J, Martin AC (2019). Structural redundancy in supracellular actomyosin networks enables robust tissue folding. Dev Cell 50, 586–598.e3.

Zusman SB, Wieschaus EF (1985). Requirements for zygotic gene activity during gastrulation in *Drosophila melanogaster*. Dev Biol 111, 359–371.